

One-step Pulsed Laser Deposition of Metal oxynitride/Carbon Composites for Supercapacitor Application

Subrata Ghosh*, Giacomo Pagani, Massimiliano Righi, Chengxi Hou, Valeria Russo, Carlo S. Casari*

Micro and Nanostructured Materials Laboratory - NanoLab, Department of Energy, Politecnico de Milano, via Ponzio 34/3, Italy

Abstract: Advanced material composite of nanocarbons and metal-based materials provides a synergistic effect to obtain excellent electrochemical charge-storage performance and other properties. Herein, 3D porous carbon-metal oxynitride nanocomposites with tunable carbon/metal and oxygen/nitrogen ratio are synthesized uniquely by simultaneous ablation from two different targets by single-step pulsed laser deposition at room temperature. Co-ablation of titanium and vanadium nitride targets together with graphite allowed us to synthesize carbon-metal oxynitride porous nanocomposite and exploit them as a binder-free thin film supercapacitor electrode in aqueous electrolyte. We show that the elemental composition ratio and hence the structural properties can be tuned by selecting target configuration and by manipulating the ablation position. We investigate how this tuning capability impacts their charge-storage performances. We anticipate the utilization of as-synthesized various composites in a single PLD production run as next-generation active materials for flexible energy storage and optoelectronic applications.

Keywords: Pulsed Laser Deposition; Metal oxynitride; Carbon; Nanocomposite; Supercapacitor; Impedance

Corresponding authors Email: subrata.ghosh@polimi.it or subrata.ghoshk@rediffmail.com (Subrata Ghosh) and carlo.casari@polimi.it (Carlo S. Casari)

1. Introduction:

3D nanostructures consisting of a high surface-to-volume ratio, plenty of active surface sites, and high edge densities, have received significant attention for their potential use in desired applications such as electrochemical energy storage, field emission, and sensors.[1][2][3] Considering supercapacitor or electrochemical capacitor technology as an example of a promising application to mitigate the global energy problem, the above-mentioned criteria are to be fulfilled where electrode materials play a pivotal role. Among the electrode materials, carbon-based materials are well-known for excellent power density, good cycle life, and electrochemical stability. They store the charge via double-layer formation at the electrode/electrolyte interface, and the energy storage device is known as electric double-layer capacitor (EDLC). In parallel, metal oxides/nitrides/oxynitrides and conducting polymers offer high specific capacitance but they have poor stability. The corresponding storage device is called pseudocapacitor since fast redox reactions occur at the surface or near the surface of the electrode to store the charge. A great effort has been made to fabricate advanced composite materials combining two types of materials, where one can get a synergistic effect from the individual constituents. For example, a composite of vertical graphene nanosheets decorated with metal oxides,[4] provided around 200 times higher areal capacitance than the vertical graphene alone.[4]

Composite materials can be prepared by one-step and multi-step processes followed by post-treatment.[5][6] In the multi-step process, considering vertical graphene/metal oxide composite as an example,[4] vertical graphene was grown by plasma-enhanced chemical vapour deposition at a relatively high temperature followed by chemical activation to functionalize, metal oxide coating by chemical route such as dip coating and annealing or hydrothermal methods.[2] In this configuration, considering the application in an electrochemical energy storage device, the top surface participates first and then the bottom structure plays a role for the diffusion of electrolytes in the bulk.[2][6] Alternatively, one-step synthesis techniques offer to grow nanostructures with more than one constituent, better bindings between the constituent elements and could offer synergistic effects more effectively while implemented as an active material for desired applications.[7] Taking the electrospinning technique as an example, one can make a homogeneous electrospun solution by adding either metal-based precursors or nanoparticles into the polymer precursor to obtain the composite after electrospinning followed by carbonizations.[8][9] These multistep processes are time-consuming, needing additional precursors and instrumental facilities, sometimes difficult to control and ensuing non-uniform and non-homogeneous distribution of each constituent.

Now-a-days, the synthesis at room temperature allows to grow nanostructures on a flexible substrate and has received significant attention for its advantage for flexible electronic applications. Although room temperature growth by thin film deposition techniques like sputtering resulted in amorphous materials, these materials also have excellent potential for energy, optoelectronic and other applications.[10][11] The interest in amorphous materials arises due to the availability of a large amount of dangling bonds, defects, free of grain boundaries and electrochemically active surface areas.[11] Among the composite materials, carbon/metal (oxy)nitride has emerged as a promising alternative to the oxide counterpart as it possesses higher electrical conductivity, better stability, and energy storage electrodes.[12] Pulsed laser deposition (PLD) stands out as one of the most versatile techniques, where one can grow varieties of nanostructures with different morphologies starting from compact to porous at room temperature.[13][14][15] However, to prepare a composite material by PLD, sequential ablation of different targets is usually employed leading to one structure on top of another,[13] or a composite target is used to get a composite structure,[14] or simultaneous ablation of multiple targets using multi-beam.[15]

Here, we proposed a unique strategy to prepare a 3D porous carbon/titanium oxynitride and carbon/vanadium oxynitride nanofoam composite by a single-step PLD production run using two different-size targets placing one into another and ablating simultaneously with a single laser beam.

We show that we can control the ratio of elemental constituents by flipping the target configuration and by manipulating the laser ablation spot position. As a potential application, the so-obtained 3D nanostructured composites are employed as energy storage electrodes and a symmetric supercapacitor device is assembled, which delivers excellent charge-storage performances.

2. Experimental methods

2.1. *Synthesis of 3D nanocomposites*

3D nanocomposites were prepared using one-step PLD technique at room temperature. The targets used for this were 1-inch and 2-inches graphite, 1-inch and 2-inches titanium nitride (TiN) and 2-inches vanadium nitride (VN). For the co-ablation from both targets simultaneously using a single laser, the smaller target was placed on the bigger one and different combinations were carried out to obtain the composite with different constituent elements content (Figure 1a). Silicon, Si (100) were used as substrates for morphological and structural characterization, whereas carbon paper substrates were used to prepare binder-free electrodes for electrochemical tests. The ablation was performed using a Nd:YAG pulsed nanosecond-laser (2nd harmonic at 532 nm, pulse duration 5-7 ns, repetition rate 10 Hz). The deposition was carried out employing two gas pressures: [16][17] 2 Pa for 2 min to grow a compact film as a buffer layer followed by 30 min deposition at 300 Pa to grow the nanofoam composite. All depositions were carried out under nitrogen background gas and the laser pulse energy was about 405 mJ with a fluence of 6.5 J/cm². Prior to deposition, the chamber was evacuated down to 10⁻³ Pa using rotary pump and turbomolecular pump. The distance between the substrate and bottom target (d_{ts1}) was 40 mm and the distance between the substrate and top target (d_{ts2}) was 34 mm (Figure 1a).

2.2. *Morphological and structural characterization.*

A field-emission scanning electron microscope (FESEM, ZEISS SUPRA 40, Jena, Germany) was employed to investigate the morphology of composite. The porosity of the nanofoam composite was estimated using SEM images by ImageJ software. Electron Dispersive X-ray spectra (EDX) were recorded at the acceleration voltage of 10 kV using Aztec software to evaluate the elemental analysis and the instrument is equipped with a Peltier-cooled silicon drift detector (Oxford Instruments). The Raman spectra of all samples were recorded by Renishaw Invia Raman spectrometer, UK. The spectra were acquired using 514 nm laser with a power of 0.4 mW, a 1800 gratings spectrometer, a 50× objective lens, and 20 accumulations with accumulation time of 10 s.

2.3 Electrochemical measurements.

The electrochemical performances of the nanocomposites were carried out in a 2-electrode configuration using Swagelok Cell (SKU: ANR-B01, Singapore) and 6M KOH used as an electrolyte. The hydrophobic PP membrane was modified by a two-step process: soaked with acetone at 20 °C for 5 min and followed by aqueous 6M KOH solution at 20 C, and used after 1 hr.[18] The cell was assembled by sandwiching separator-soaked-electrolytes between the nanocomposites grown on carbon paper. Prior to the test, nanocomposite electrodes and a modified separator were dipped into the electrolyte solution for several hours. Cyclic voltammogram, charge-discharge test and electrochemical impedance spectra were recorded using a PALMSENS electrochemical workstation. Before recording the original data, the proto-type cells were scanned at 100 mV/s scan rate for 1000 cycles. The cyclic voltammetry at different scan rates ranging from 20 to 1000 mV/s and charge-discharge at different current densities of 150 to 500 μA were carried out. The areal capacitance was calculated using the equation: $C_{areal} = \int I dv / Av\Delta V$, where I is the current, v is the scan rate, A is the geometric area of the electrode and ΔV is the voltage of the device. Single electrode capacitance

= $4 \times$ device capacitance. The volumetric capacitance of electrode materials was estimated by dividing the areal capacitance by the total height of two symmetric nanocomposite electrodes. The electrochemical impedance spectroscopy was conducted in the frequency range of 1 Hz to 0.1 MHz at open circuit potential with a 10 mV *a.c.* perturbation. The specific capacitance at 120 Hz is calculated using the relation of $C_s = 1/2\pi fZ''A$. The relaxation time constant (τ_0) was estimated from the corresponding frequency (f_0) at -45° phase angle using the equation of $f_0 = 1/\tau_0$. The resistor-capacitor time constant at a frequency (f) of 120 Hz was calculated using the relation of $\tau_{RC} = Z'/2\pi fZ''$, where Z' and Z'' are the real and imaginary impedance, respectively.

3. Result and Discussions:

3.1. Carbon-Ti oxynitride composites

The C/Ti oxynitride composite nanofoam (C/TiO_xN_y) is prepared by placing a 1-inch TiN target on top of a 2-inch graphite target and ablated at 250 Pa of pressure ((Figure 1a). The morphology is found to be porous (Figure 1b) with a porosity of 81.55% and an average uniform height of 6.4 μm (Figure 1c). From the cross-sectional image (Figure 1c), the nanofoam composite consists of a compact layer on the substrate with a porous structure on top. The compact layer provides better adhesion with the current collector, excellent conductivity, and complementary capacitance, whereas the porous structure provides a large specific surface area and open porous structures for fast electrolyte ion transport.[19] The basic constituents of C/TiO_xN_y from top-view EDX measurement (Figure 1d) are carbon (48.7 at.%), titanium (Ti, 7.7 at.%), nitrogen (N, 16.3 at.%) and oxygen (O, 27.3 at.%). Figure 1(e-h) shows the cross-sectional electron image and corresponding elemental mapping, which confirms the uniform distribution of each element in the nanofoam composite. Although pure nitrogen was used as background gas during the ablation, the presence of inevitable oxygen in the composite is attributed to adventitious oxygen and native thin oxide layer formation on the porous nanocomposite upon air exposure.

Figure 1(i) shows the Raman spectrum of C/TiO_xN_y, which consists of sp^2 -carbon band with two components namely, D-peak (located at 1372 cm^{-1}) and G-peak (located at 1585 cm^{-1}). The D-peak is attributed to the breathing mode of hexagonal rings, and it is related to disorder in the structure, and G-peak is due to the carbon-carbon stretching mode of sp^2 -carbon. Other carbon peaks found were sp -carbon located at 2170 cm^{-1} and second orders in the range of 2500 to 4000 cm^{-1} . The huge photoluminescence (PL) background, as can be seen from the Raman spectra, is quite dominating and can be attributed to the adsorbed water on the light density and porous carbon-based nanostructures[20] and the presence of metallic Ti-components. In the study of wide range of hydrogenated amorphous carbons, the normalized PL slope is found to be increases exponentially with the hydrogen content.[20] The normalized PL slope is estimated from the ratio of slope in the linear region of 1000-1900 cm^{-1} (in the unit of cm) and height of the G-peak (Figure 1(i)).[20] With the same analogy, to provide a quantitative measure of metallic components' influence in the lightweight porous structure, the normalized PL slope estimated is 7.46 μm , which is much higher than the amorphous carbon nanofoam (3.5-4.3 μm).[21] This huge PL background is also one of the reason behind negligible contribution of oxynitride in Raman spectra. Another factor is amorphous nature of structure as the structure has grown at room temperature and high deposition pressure of 250 Pa.[22] Since the structure is amorphous, it shows broadened G-peak with full-width a half maximum of 134.6 cm^{-1} (Table 1).

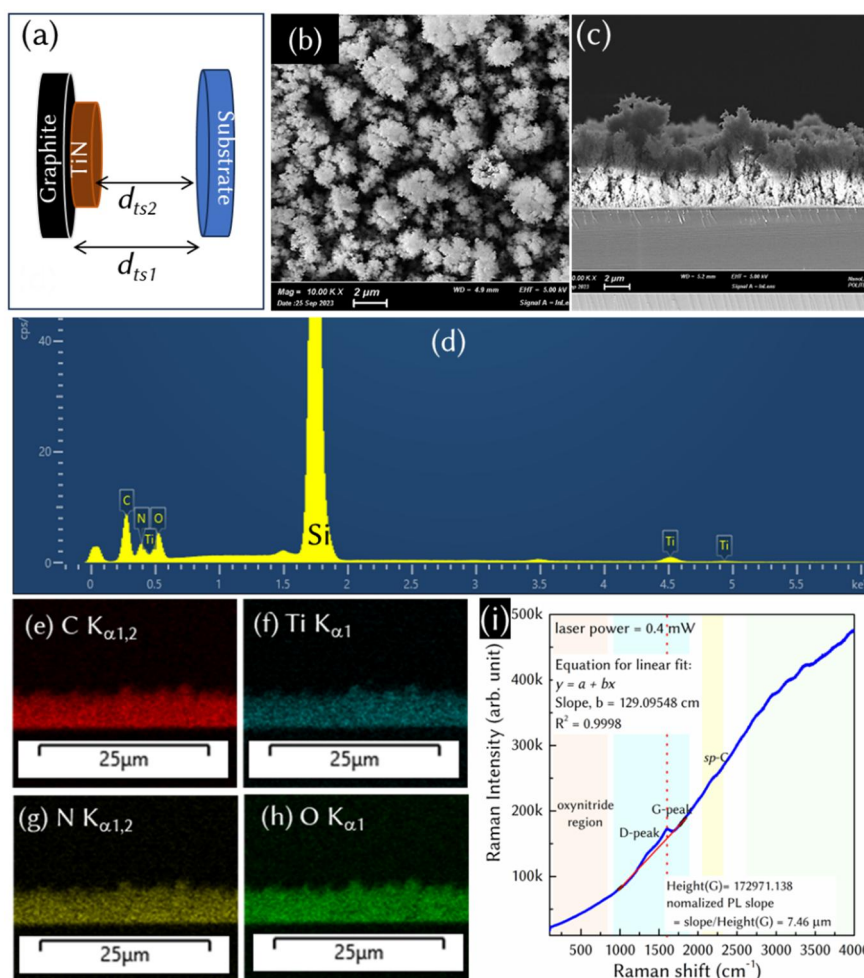


Figure 1: Morphology and structure of Carbon-titanium oxynitride $C-TiO_xN_y$. (a) schematic of two-target assembly for the deposition in PLD. (b) Top view and (c) cross-sectional scanning electron micrograph, (d) EDX spectra, (e) electron image, and elemental mapping of (f) carbon, (g) vanadium, (h) nitrogen, and (i) oxygen. Raman spectra of nanofoam composite with 514 nm laser

As-grown nanofoam composite on the carbon paper substrate is used as a binder-free electrode in a supercapacitor. The performance of the C/TiO_xN_y symmetric device is shown in Figure 2. The cyclic voltammogram (CV) profile for the C/TiO_xN_y device is found to be mirror-symmetric and unchanged near-rectangular in shape even at the higher scan rate (Figure 2a). Deviation from perfect rectangular CV can be attributed to the pseudocapacitive contribution from oxynitride and functional groups of carbon along with the double-layer capacitive contribution of carbons. The plot of the areal and volumetric capacitance of C/TiO_xN_y with respect to the scan rate is shown in Figure 2b. The areal capacitance of the device is found to be 0.61 mF/cm^2 at the scan rate of 0.1 V/s and it retains 50% at a high scan rate of 1 V/s . The areal capacitance of single electrode of 2.4 mF/cm^2 at 0.1 V/s , which is obtained by multiplying the device areal capacitance by 4, is found to be comparable with many reports such as vertical graphene nanosheets (0.197 mF/cm^2),^[23] $Ni_3(HHTP)_2$ @woven fabrics (0.205 mF/cm^2), TiO_2 nanogrid (0.74 mF/cm^2)^[24] and titanate hydrate nanogrid (0.08 mF/cm^2).^[24] Moreover, the cycle stability of the device is found to be 86% at $100 \mu\text{A}$ even after 10000 charge-discharge cycles, indicating good electrochemical stability. The inset of Figure 2c shows the charge-discharge profile of the device for a few cycles. In order to explore the charge-storage kinetics, electrochemical impedance spectroscopic results are investigated through the Nyquist and Bode plot.^[25] At 120 Hz, the negative phase angle of the device is found to be 52° and the specific capacitance is estimated to be $91 \mu\text{F/cm}^2$ with good frequency response (Figure 2d). The obtained

specific capacitance of our nanofoam composite at 120 Hz is found to be impressive, it is outperforming than P/N-doped carbon ($30 \mu\text{F}/\text{cm}^2$), [26] vertically oriented graphene ($87 \mu\text{F}/\text{cm}^2$) [27] and it is comparable to the existing reports on B/N-doped carbon ($99 \mu\text{F}/\text{cm}^2$) and, laser processed carbon-titanium carbide heterostructure ($118 \mu\text{F}/\text{cm}^2$) [19] based devices. On over that, the negative phase angle of our device at 120 Hz is comparable and/or better than N-doped mesoporous carbon (0°) [28], activated carbon-based commercial electric double layer capacitor (0°) [29], [30], thermally reduced graphene oxide (30°) [31], 3D ordered porous graphene film (53°) [32], etc. Moreover, it has been demonstrated for NiTe_2 -based devices that the phase angle around 53° is sufficient for the AC line filtering purpose. [33] This result suggests that the nanofoam composite not only has good charge-storage properties but also can be used for filtering applications. The elemental composition ratio is manipulated by flipping the targets and then changing the ablation spot to improve the charge-storage performance further, which is detailed in the following.

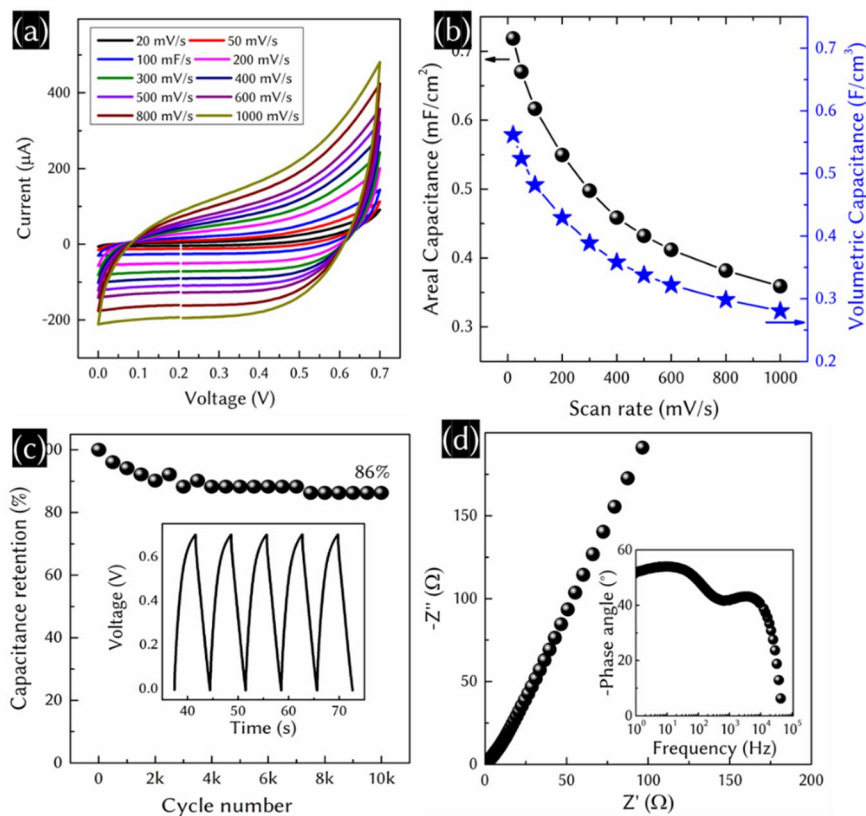


Figure 2: Supercapacitor performance of Carbon-Titanium oxynitride. (a) cyclic voltammogram at different scan rates, (b) areal and volumetric capacitance with respect to the scan rate, (c) cycle stability with the charge-discharge cycles at $100 \mu\text{A}$ in an inset, (d) Nyquist plot with Bode plot in the inset.

To explore such possibilities, we flipped the target compared to the previous case by placing the 1-inch graphite target on the 2-inch TiN target (Figure 3a) at first and then changed the position of ablation spot slightly (Figure 3b). The ablation was carried out at 250 Pa pressure keeping other deposition parameters the same. With our set-up, the ablation spot can be changed by 1 mm precisely and depositions are carried out at three different ablation spots. Prior to this, let us discuss the different zones of plasma plume for the case of ablation in a single target (Figure 3c) for better visualization of three deposition processes and their consequences. The plasma plume consists of hot core, mid regions and cold regions followed by shock wavefronts. In the mid-region, where ions and neutral coexist due to the ionization and recombination, we can see two different bright zones for

the case of co-ablation: one is coming from the bottom target, and another is from the top (Figure 3d-f). For the sake of simplicity, we define the length of those two bright zones as L_1 for the top target and L_2 for the bottom one. It can be easily seen that if one changes the ablation spot position slightly, the relative ratio of L_1 and L_2 can be controlled, which also has an impact on the final structure obtained.

Case I: the ablation position is more on the carbon side as a result $L_1 > L_2$ (Figure 3d)

Case II: the ablation position in the middle of the boundary, where $L_1 \approx L_2$ (Figure 3e)

Case III: the ablation is more on TiN such that $L_1 < L_2$ (Figure 3f)

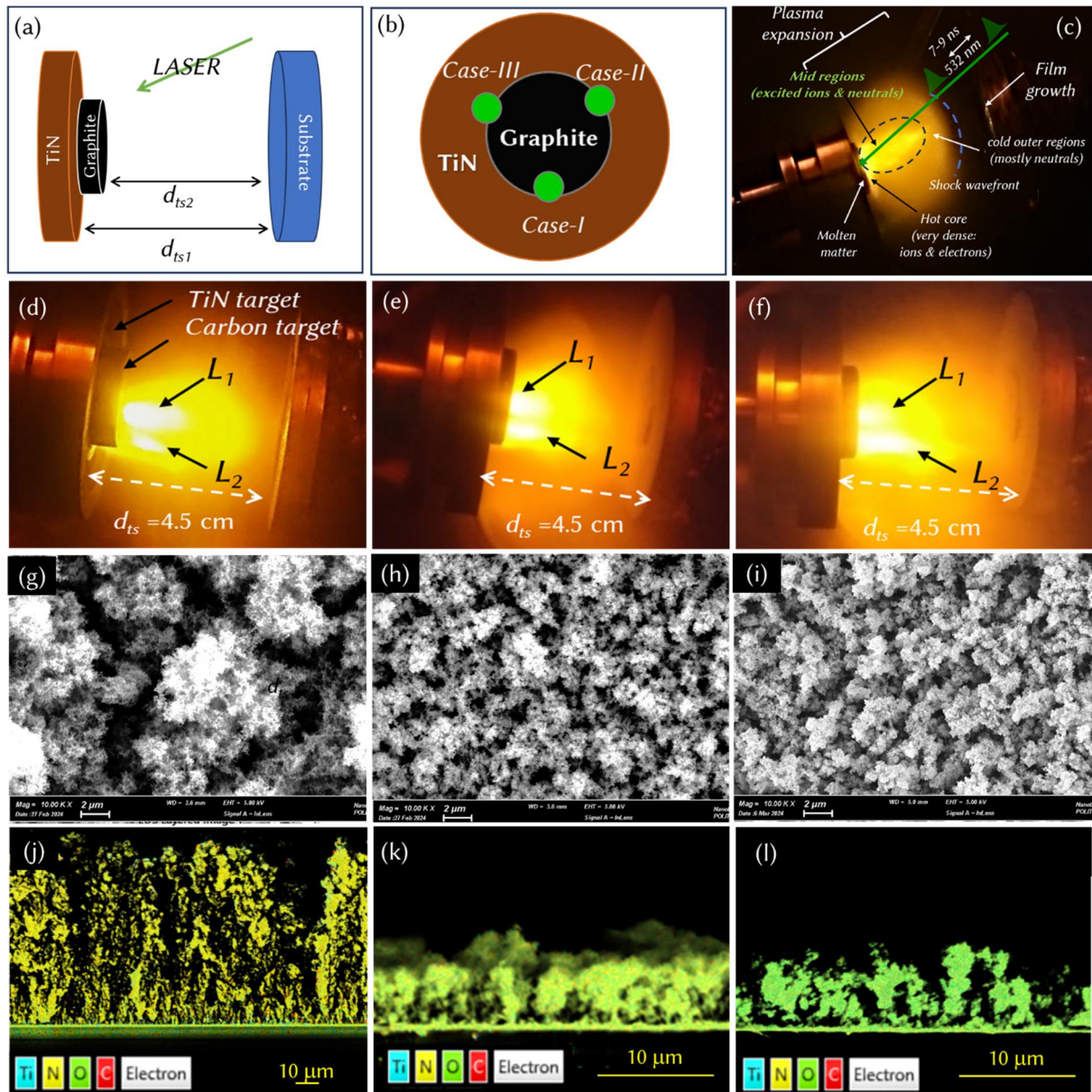


Figure 3: (a) Schematic of targets assembly and (b) three ablation spots. (c) Photographic image of plasma plume for single target ablation by 532 nm laser demarcating different zones of plasma. (d-f) Representative photographic image of plasma plume for three different ablation conditions. Corresponding (g-i) scanning electron micrographs, (j-l) elemental layered image.

For $L_1 > L_2$ (Figure 3b and 3f), since the ablation spot is more on the graphite target side, the ablation yield of carbon is much higher than that of TiN and $d_{ts\text{-graphite}}$ is less than the $d_{ts\text{-TiN}}$. As a result, the average growth rate of the final composite is found to be 2.34 $\mu\text{m}/\text{min}$ (Figure 3j). As the ablation

position shifted towards the TiN target, the growth rate was found to be reduced to 0.2 $\mu\text{m}/\text{min}$ for the other two cases (Figure 3f-g). The morphology (Figure 3g-i), of C/TiO_xN_y-1 is more porous and C/TiO_xN_y-3 possesses a relatively higher density of nanoparticles. The porosity is found to be decreased from 90% (C/TiO_xN_y-1) to 67% (C/TiO_xN_y-3) as the ablation spot shifted from the graphite-rich zone to the TiN-rich zone. The maximum height of the film for C/TiO_xN_y-1, C/TiO_xN_y-2, and C/TiO_xN_y-3 is found to be 81.2, 8.1 and 7.9 μm , respectively. The corresponding cross-sectional elemental layered image is shown in Figure 3(j-l) and the elemental mapping of each element for all composites is given in Figure S(1-3) in the supplementary file, which confirms the uniform and homogeneous distribution of each elements in the nanofoam. From the elemental compositional analysis, as obtained from the top-view EDS result, C/TiO_xN_y-1 contains higher carbon content with 86.3 at.% and less Ti-content about 1.4 at.% along with oxygen and nitrogen content, which is obvious as explained before. Whereas, C/TiO_xN_y-2 and C/TiO_xN_y-3 contain Ti(carbon) of 22.9 (24.3) and 31.4 (4.0) at.%, respectively since the laser ablation spot was shifted towards the nitride-side maintaining the condition of co-ablation from both targets. Strikingly, the maximum oxygen content (61.1 at.%) has been seen for C/TiO_xN_y-3 compared to that of C/TiO_xN_y-2 (43.9 at.%), as a higher amount of Ti is prone to physisorbed atmospheric oxygens more. Although the ablation spot position is same, the higher Ti-content of C/TiO_xN_y-2 (22.9 at.%) compared to that of C/TiO_xN_y (7.7 at.%) is attributed to the arrangement of targets as the TiN target was placed below the graphite target for the former case. For the C/TiO_xN_y composite, increasing Ti- and N-content or decreasing carbon content also leads to an increase in the amount of oxygen content. Increasing N-content would improve the electrochemical stability whereas O-content may contribute more pseudocapacitance to the double-layer capacitance when the composite is explored as an energy storage electrode.

The Raman spectra of all composites are shown in Figure 4(a-b). In the Raman spectra of C/TiO_xN_y-1, the D-peak and G-peak are quite prominent (Figure 4b), and the spectra contain a lower photoluminescence background (normalized PL slope of 1.21 μm) and very weak contribution from TiO_xN_y as C/TiO_xN_y-1 contains high carbon content. In low frequency region (100 to 1000 cm^{-1}) of Raman spectra of C/TiO_xN_y-1 (Figure 4c), we observed two large bands, which are compatible with amorphous titanium oxynitride as reported in the literature.[22] Raman spectra of C/TiO_xN_y-2 (Figure 4a) show D- and G-peak with huge amount of PL background (normalized PL slope of 5.98 μm), which is similar to the C/TiO_xN_y (Figure 1i) and expected due to the same target assembly except flipping. However, the relative ratio of constituent elements is different for those two cases, which reflects in normalized PL slope, FWHM of G-peak and I_D/I_G ratio (table 1). For C/TiO_xN_y-3, one can easily see the dominance of oxynitride over the carbon contribution in the Raman spectra of with a normalized PL slope of 3.66 μm , which is in agreement with EDX result. It should be noted that an additional peak appeared in the middle of D-peak and G-peak (Figure 4b), which can be due to higher amount oxygen presence in the structure (also confirmed from EDX, table 1).[34][35] To know more about the structural changes in the nanofoam composites prepared at different ablation spots, the FWHM of G-peak and I_D/I_G are estimated and found to be decreased from the C/TiO_xN_y-1 to C/TiO_xN_y-3, which can be attributed to the improvement in the structure of nanofoam composite and different stoichiometry of individual elements (table 1). Thus, it is clear from the Raman spectroscopic analysis that all nanofoam composites very disordered, amorphous and combination of carbon and Ti-oxynitride, and they have different structural quality since they consist of different amount of elemental compositions, which is consistent with the EDX result.

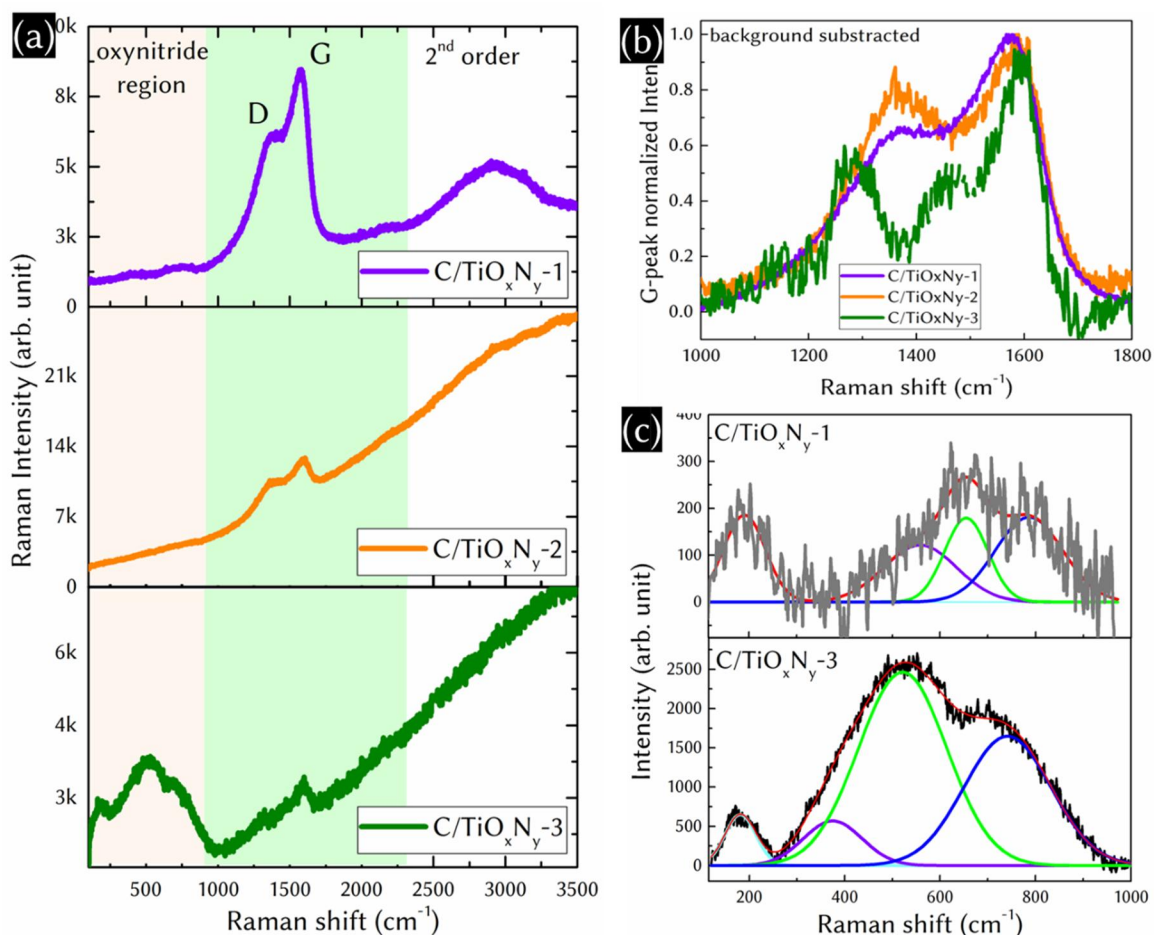


Figure 4: (a) Visible Raman spectra of C/TiO_xN_y-1 , C/TiO_xN_y-2 , and C/TiO_xN_y-3 . The wavenumber range of 100 to 3500 cm^{-1} is selected to show the photoluminescence background for all composites. (b) background subtracted and G-peak normalized Raman spectra in the range of 1000 to 1800 cm^{-1} of the nanofoam composites. To reduce the signal-to-noise ratio, the Raman spectra of C/TiO_xN_y-3 was recorded for quite long accumulations and smoothed compared to other two. (c) background corrected and fitted Raman spectra of nanofoam composite in the oxynitride zone with deconvoluted peaks.

The charge-storage performances of all supercapacitor devices using the above three composites were carried out in a symmetric configuration. The cyclic voltammogram at different scan rates and charge-discharge profile at different current densities for all composites are provided in Figure S4 of the supplementary file. A comparative volumetric CV of all three devices at 0.5 V/s is shown in Figure 5(a). Among all, C/TiO_xN_y-2 supercapacitor device shows the highest area under the CV curve, while normalized with the height of the films (Figure 5(a) and table 1). The highest areal capacitance at 0.1 V/s is obtained for C/TiO_xN_y-1 (1.85 mF/cm^2) supercapacitor with an electrode height of around 75 μm (Figure 5(b)). Whereas highest volumetric capacitance of 1760 mF/cm^3 at 0.1 V/s is obtained from C/TiO_xN_y-2 device. However, the C/TiO_xN_y-3 supercapacitor device shows better rate performance and cycle stability (Figure 5(b-c)). This can be attributed to the composition and its structure as explained in EDX and Raman spectroscopic results. As seen from Figure 5c, a rise in capacitance (~120%) observed in the first 2000 cycles for the C/TiO_xN_y-2 supercapacitor can be attributed to the electrochemical activation and active nitrogen and titanium vacancies. While looking at the impedance spectra (Figure 5d), C/TiO_xN_y-2 supercapacitor device exhibited lower equivalent series resistance, steeper line at low-frequency region, higher phase angle at 120 Hz, smaller relaxation and capacitor-resistor time constant and higher specific capacitance at 120 Hz compared to that of C/TiO_xN_y-1 and C/TiO_xN_y-3 supercapacitor (table 1). This result suggests that C/TiO_xN_y-2 consists of optimized compositional elements and structural quality.

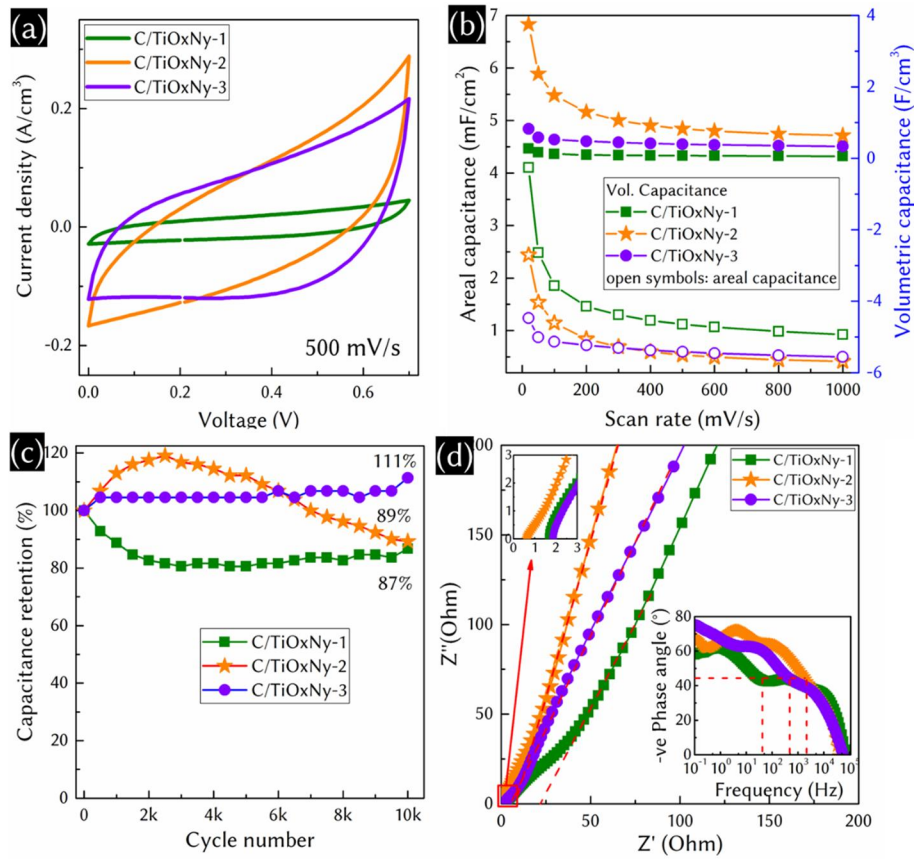


Figure 5: Supercapacitor performance of Carbon-Titanium oxynitride. (a) volumetric cyclic voltammogram at 0.5 V/s, (b) areal and volumetric capacitance at different scan rates, (c) cycle stability over 10000 charges-discharges, (d) Nyquist plot, top inset represent Nyquist plot at high-frequency zone demarcating equivalent series resistance obtained from the plot at zero Z'' -axis and lower inset represent the Bode plot. Dashed lines in each Nyquist plot crossing the zero Z'' -axis represent charge-transfer resistance. Dashed red lines in the phase angle represent the characteristic frequency at -45° phase angle.

Table 1: Physico-chemical and charge-storage properties of C/MO_xN_y composites (M stands for Ti and V). The charge-storage performances were carried out in a 6M KOH electrolyte.

Nanofoam composite (C: carbon)	Avg. Height of film (μm), porosity	C/M/N/O (at.% from EDX; M: Ti and V)	Photoluminescence background (μm)	Full width at half maxima (FWHM) of/G (cm ⁻¹)	Intensity ratio of D-to-G	Vol. (areal) capacitance in mF/cm ³ (mF/cm ²), Rate performance, cycle stability after 10k cycles of composite	Area specific Capacitance (μF/cm ²) at 120 Hz	Phase angle at 120 Hz	Relaxation time constant in ms (frequency in Hz) at -45°	Capacitor-Resistor time constant (ms) at 120 Hz	Equivalent series resistance (Ω)
C/TiO _x N _y	6.4, 81.55%	48.7/7.7/16.3/27.3	7.6	134.6	0.89	480 (0.61) at 0.1 V/s, 58.3% at 1 V/s, 86% at 100 μA	91	-53°	4.7 (209.7)	0.98	0.6
C/TiO _x N _y -1	75, 90.02%	86.3/1.4/3.3/9.0	1.21	117.0	0.82	124 (1.85) at 0.1 V/s, 50% at 1V/s, 87% at 125 μA	78	-43°	40 (24.8)	1.39	1.7
C/TiO _x N _y -2	6.5, 88.72%	24.3/22.9/8.8/43.9	5.98	111.0	0.79	1763 (1.14) at 0.1 V/s, 36% at 1 V/s, 89% at 125 μA	109	-63°	0.6 (1643.6)	0.67	0.7
C/TiO _x N _y -3	7.5, 67.13%	4.0/31.4/3.5/61.1	3.66	96.6	0.58	526 (0.78) at 0.1 V/s, 63% at 1 V/s, 111% at 125 μA	82	-53°	2.7 (363.8)	0.96	1.9
C/VO _x N _y -2	18, 60.37%	46.3/10.7/19.9/23.1	2.78	151.8	0.69	260 (0.96) at 0.1 V/s, 48% at 1 V/s, 71% at 100 μA	132	-51°	8.1 (123.3)	1.3	0.6

3.2. Carbon-V oxynitride composites

As can be seen from previous investigations that C/TiO_xN_y-2 has better charge-storage performance, we attempted to replace TiN by VN target with same configuration. This approach also helps to showcase the versatility of our strategy. In which, a 1-inch graphite target was placed on VN target with a diameter 2-inch to co-ablate simultaneously at the pressure of 250 Pa and other deposition parameters were the same (Case-II, similar to Figure 3a. See details in experimental section). Moreover, VN nanocrystalline structures has high charge storage capacitance of 1340 F/g at 2 mV/s and it can be operated within the electrochemical stability window of -1.2 to 0V vs reference electrode in aqueous electrolyte medium.[36] Thus, VN-based became a popular choice to be used as negative electrode in asymmetric supercapacitor device, which is the major boost to obtain higher energy density of supercapacitor device. However, major problem with vanadium nitride nanostructures is electrochemical stability and hence there is urgent need of designing composite with carbon.[12] The 3D porous morphology of nanofoam composite (C/VO_xN_y-2) is confirmed from the electron micrographs (Figure 6a) with a porosity of 60% and the average height of the film in the uniform region is found to be. Compared to the C/TiO_xN_y-2 (average height of 6.5 μm), the higher average height of the film of 18 μm (inset of Figure 6a) with the same target-assembly configuration (case-II) is attributed to the higher ablation yields of VN than that of TiN.

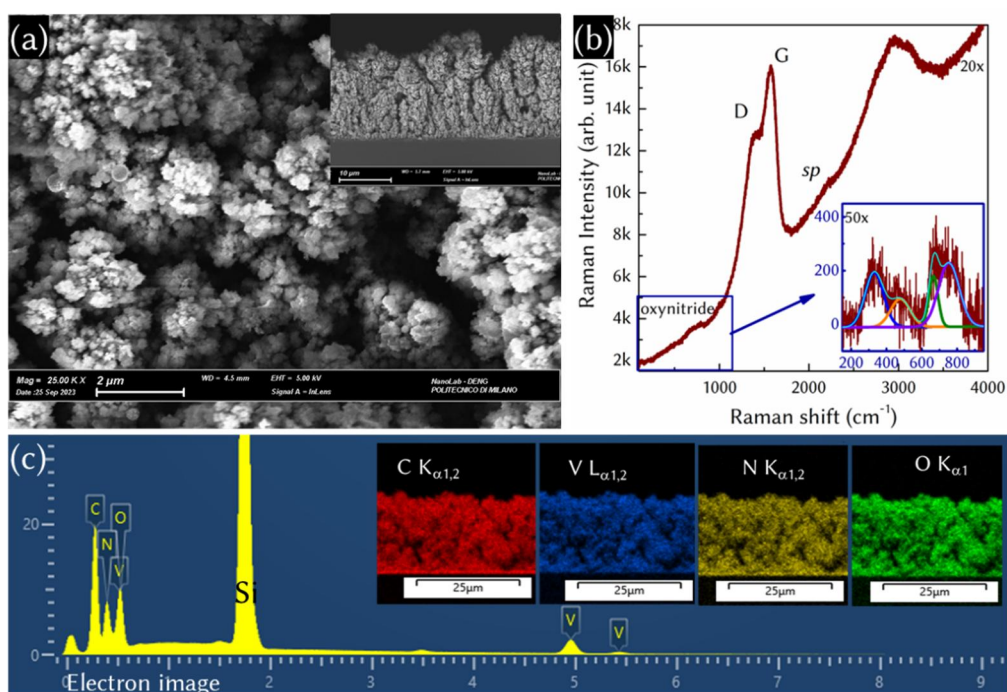


Figure 6: **Morphology and structure of Carbon-vanadium oxynitride.** (a) Scanning electron micrograph, (b) Raman spectra of nanofoam composite with low-frequency range spectra accumulated for higher time at inset. (c) EDX spectra, (d) electron image, and elemental mapping of (e) carbon, (f) vanadium, (g) nitrogen, and (h) oxygen.

The Raman spectrum of the film is shown in Figure 6b. It consists of a weak peak in the low-frequency zone of 100 to 1000 cm⁻¹, and sp²-carbon peaks with second-order counterpart, and a weak sp-carbon peak. The low frequency region consists of two broad bands, which is compatible with amorphous vanadium oxynitride.[37] Thus, the Raman spectra of C/VO_xN_y confirms the co-existence of functionalized amorphous nanocarbons and vanadium oxynitride. Figure 6c shows the EDX spectra

of C/VO_xN_y-2 , which consists of 46.3 at.% carbon, 10.7 at.% vanadium, 19.9 at.% nitrogen and 23.1 at.% oxygen. The EDX result again confirms that the sputtering yield for C/VO_xN_y-2 (elements at.% ratio of $C/V = 4.33$ and $V/N = 0.54$) is completely different than the C/TiO_xN_y-2 (elements at.% ratio of $C/Ti = 1.06$ and $Ti/N = 2.6$). The corresponding cross-sectional elemental mapping (Figure 6d-g) of C/VO_xN_y-2 confirms the uniform distributions of each element in the nanofoam composite.

The electrochemical charge-storage performance of the C/VO_xN_y-2 composite is carried out by fabricating a symmetric cell. The CV of the nanofoam composite is shown in Figure 7a. The maximum areal (volumetric) capacitance of the nanofoam composite device obtained at 0.1 V/s is 0.96 mF/cm² (260 mF/cm³) and retains 48% capacitance at 1 V/s (Figure 7b). The areal capacitance of the nanofoam composite is found to be 3.7 mF/cm² at 0.1 V/s. While running for 10000 charge-discharge cycles, the symmetric device delivered 71% specific capacitance with respect to the first cycle (Figure 7c). The inset of Figure 7c shows the charge-discharge profile of the device found to have poor Coulombic efficiency compared to our Ti-based nanofoam composite shown above. The poor electrochemical stability and Coulombic efficiency of vanadium-based materials is one of the common problems. To evaluate charge-storage kinetics, the impedance spectra of the nanofoam composite is recorded and shown in Figure 7d. The negative phase angle of nanofoam is found to be 51° at 120 Hz. Whereas the specific capacitance of C/VO_xN_y-2 at 120 Hz is found to be 132 μF/cm², which is the highest among all studied nanofoam composites. The performance can be improved further by tuning the elemental compositions again as like C/TiO_xN_y nanofoam composite or post-treatment.

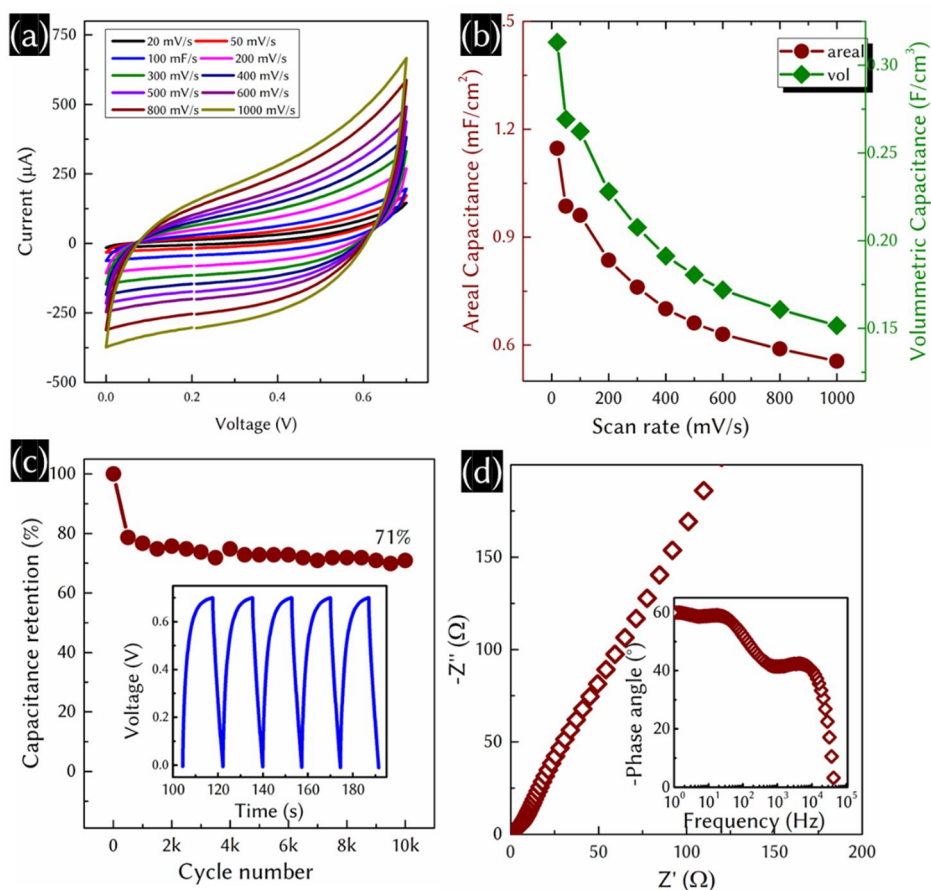


Figure 7: Supercapacitor performance of Carbon-vanadium oxynitride. (a) cyclic voltammogram at different scan rate, (b) areal and volumetric capacitance with respect to the scan rate, (c) cycle stability with the charge-discharge cycles at xx current density in inset, (d) Nyquist plot with Bode plot in inset.

4. Conclusion

In summary, we successfully demonstrated the co-ablation of two different targets simultaneously to synthesize the 3D porous carbon/metal oxynitride composite in one-step pulsed laser deposition with the single laser. The ratio of constituents' elements in the composites is manipulated by changing the laser ablation position and the different ratio of elements in the composites is attributed to the different sputtering yield of the target materials. Finally, we showed that the 3D porous nanocomposites have the potential to be used as binder-free and conductive agent-free electrochemical energy storage electrodes and the composites prepared by this adaptable strategy are summarized in [Table 1](#). In comparison, the nanofoam composite with optimized constituent elements (carbon, titanium, oxygen, and nitrogen) showed the highest volumetric capacitance of 1763 mF/cm³ at 0.1 V/s with high-frequency response compared to other nanofoam composites. Whereas vanadium-based nanofoam composite exhibited highest specific capacitance of 132 μF/cm² at 120 Hz. The charge-storage performance can be improved further by post-treatment of an electrode, which is the subject of our ongoing research. These results ensure that by controlling the ratio of elemental constituents of the composite, morphology, and growth rate one can optimize the structural and charge-storage properties for electrochemical energy storage applications and other desired applications.

Authors contributions

S.G. and C.S.C. planned and conceptualized the work. S. G., G.P. and C.H. performed the PLD deposition. S. G. and G. P. performed Raman spectroscopy of samples. S. G. M.R. and G.P. did the electrochemical measurements and assisted in the analysis. V.R. contributed to Raman spectroscopic analysis. S. G. wrote the manuscript. All authors revised the manuscript and approved the final version of the manuscript.

Notes

The authors declare no competing financial interest.

ACKNOWLEDGEMENT

S.G thank Horizon Europe (HORIZON) for the Marie Skłodowska-Curie Fellowship (grant no. 101067998-ENHANCER). Carlo S. Casari acknowledges partial funding from the European Research Council (ERC) under the European Union's Horizon 2020 Research and Innovation Program ERC Consolidator Grant (ERC CoG2016 EspLORE Grant Agreement 724610, website: www.esplora.polimi.it). Carlo S. Casari also acknowledges funding by the project funded under the National Recovery and Resilience Plan (NRRP), Mission 4 Component 2 Investment 1.3 Call for Tender 1561 of 11.10.2022 of Ministero dell'Università e della Ricerca (MUR), funded by the European Union NextGenerationEU Award Project Code PE0000021, Concession Decree 1561 of 11.10.2022 adopted by Ministero dell'Università e della Ricerca (MUR), CUP D43C22003090001, Project "Network 4 Energy Sustainable Transition (NEST)".

DATA AVAILABILITY: All the data of this study are available in the main manuscript and the Supplementary Information.

References:

- [1] Tontini G, Greaves M, Ghosh S, Bayram V and Barg S 2020 MXene-based 3D porous macrostructures for electrochemical energy storage *J. Phys. Mater.* **3** 022001
- [2] Zheng S, Shi X, Das P, Wu Z-S and Bao X 2019 The Road Towards Planar Microbatteries and Micro-Supercapacitors: From 2D to 3D Device Geometries *Adv. Mater.* **31** 1900583
- [3] Kumar S, Saeed G, Zhu L, Hui K N, Kim N H and Lee J H 2021 0D to 3D carbon-based networks combined with pseudocapacitive electrode material for high energy density supercapacitor: A review *Chem. Eng. J.* **403** 126352
- [4] Ghosh S, Polaki S R, Sahoo G, Jin E-M, Kamruddin M, Cho J S and Jeong S M 2019 Designing metal oxide-vertical graphene nanosheets structures for 2.6 V aqueous asymmetric electrochemical capacitor *J. Ind. Eng. Chem.* **72** 107–16
- [5] Ghosh S, Polaki S R, Macrelli A, Casari C S, Barg S, Jeong S M and Ostrikov K (Ken) 2022 Nanoparticle-enhanced multifunctional nanocarbons—recent advances on electrochemical energy storage applications *J. Phys. D. Appl. Phys.* **55** 413001
- [6] Bayatsarmadi B, Zheng Y, Casari C S, Russo V and Qiao S-Z 2016 Pulsed laser deposition of porous N-carbon supported cobalt (oxide) thin films for highly efficient oxygen evolution *Chem. Commun.* **52** 11947–50
- [7] Jo M S, Ghosh S, Jeong S M, Kang Y C and Cho J S 2019 Coral-Like Yolk–Shell-Structured Nickel Oxide/Carbon Composite Microspheres for High-Performance Li-Ion Storage Anodes *Nano-Micro Lett.* **11** 1–18
- [8] Young Jeong S, Ghosh S, Kim J-K, Kang D-W, Mun Jeong S, Chan Kang Y and Cho J S 2019 Multi-channel-contained few-layered MoSe₂ nanosheet/N-doped carbon hybrid nanofibers prepared using diethylenetriamine as anodes for high-performance sodium-ion batteries *J. Ind. Eng. Chem.* **75** 100–7
- [9] Ghosh S, Yong W D, Jin E M, Polaki S R, Jeong S M and Jun H 2019 Mesoporous carbon nanofiber engineered for improved supercapacitor performance *Korean J. Chem. Eng.* **36** 312–320
- [10] Kim I, Shim C, Kim S W, Lee C, Kwon J, Byun K and Jeong U 2023 Amorphous Carbon Films for Electronic Applications *Adv. Mater.* **35** 2204912
- [11] Kang J, Yang X, Hu Q, Cai Z, Liu L-M and Guo L 2023 Recent Progress of Amorphous Nanomaterials *Chem. Rev.* **123** 8859–941
- [12] Ghosh S, Jeong S M and Polaki S R 2018 A review on metal nitrides/oxynitrides as an emerging supercapacitor electrode beyond oxide *Korean J. Chem. Eng.* **35** 1389–408
- [13] Mao S S and Zhang X 2015 High-Throughput Multi-Plume Pulsed-Laser Deposition for Materials Exploration and Optimization *Engineering* **1** 367–71
- [14] Grant-Jacob J A, Prentice J J, Beecher S J, Shepherd D P, Eason R W and Mackenzie J I 2018 Particulate reduction in ternary-compound film growth via pulsed laser deposition from segmented binary-targets *Mater. Res. Express* **5** 036402
- [15] Darwish A M, Sarkisov S S and Patel D N 2016 Concurrent Multi-Target Laser Ablation for Making Nano-Composite Films *Applications of Laser Ablation - Thin Film Deposition, Nanomaterial Synthesis and Surface Modification* (InTech)
- [16] Nakamura D, Shimogaki T, Nakao S, Harada K, Muraoka Y, Ikenoue H and Okada T 2014 Patterned growth of ZnO nanowalls by nanoparticle-assisted pulsed laser deposition *J. Phys. D. Appl. Phys.* **47** 034014

- [17] El Zein B, Boulfrad S, Jabbour G E and Dogheche E 2014 Parametric study of self-forming ZnO Nanowall network with honeycomb structure by Pulsed Laser Deposition *Appl. Surf. Sci.* **292** 598–607
- [18] Ciszewski A and Rydzyńska B 2007 Studies on self-assembly phenomena of hydrophilization of microporous polypropylene membrane by acetone aldol condensation products: New separator for high-power alkaline batteries *J. Power Sources* **166** 526–30
- [19] Zhang Z, Wang Z, Wang F, Qin T, Zhu H, Liu P, Zhao G, Wang X, Kang F, Wang L and Yang C 2023 A Laser-Processed Carbon-Titanium Carbide Heterostructure Electrode for High-Frequency Micro-Supercapacitors *Small* **19** 2300747
- [20] Casiraghi C, Ferrari A C and Robertson J 2005 Raman spectroscopy of hydrogenated amorphous carbons *Phys. Rev. B* **72** 085401
- [21] Ghosh S, Righi M, Macrelli A, Orecchia D, Maffini A, Goto F, Bussetti G, Dellasega D, Russo V, Bassi A L and Casari C S 2024 Ballistic-aggregated Carbon Nanofoam in Target-side of Pulsed Laser Deposition for Energy Storage Applications *arXiv:2405.08957*
- [22] Bricchi B R, Mascaretti L, Garattoni S, Mazza M, Ghidelli M, Naldoni A and Li Bassi A 2022 Nanoporous Titanium (Oxy)nitride Films as Broadband Solar Absorbers *ACS Appl. Mater. Interfaces* **14** 18453–63
- [23] Ghosh S, Mathews T, Gupta B, Das A, Gopala Krishna N and Kamruddin M 2017 Supercapacitive vertical graphene nanosheets in aqueous electrolytes *Nano-Structures & Nano-Objects* **10** 42–50
- [24] Wang Z, Li Z and Zou Z 2015 Application of binder-free TiO_xN_{1-x} nanogrid film as a high-power supercapacitor electrode *J. Power Sources* **296** 53–63
- [25] Laschuk N O, Easton E B and Zenkina O V. 2021 Reducing the resistance for the use of electrochemical impedance spectroscopy analysis in materials chemistry *RSC Adv.* **11** 27925–36
- [26] Han Z J, Huang C, Meysami S S, Piche D, Seo D H, Pineda S, Murdock A T, Bruce P S, Grant P S and Grobert N 2018 High-frequency supercapacitors based on doped carbon nanostructures *Carbon N. Y.* **126** 305–12
- [27] Miller J R, Outlaw R A and Holloway B C 2010 Graphene Double-Layer Capacitor with ac Line-Filtering Performance *Science (80-.).* **329** 1637–9
- [28] Lin T, Chen I-W, Liu F, Yang C, Bi H, Xu F and Huang F 2015 Nitrogen-doped mesoporous carbon of extraordinary capacitance for electrochemical energy storage *Science (80-.).* **350** 1508–13
- [29] Taberna P L, Simon P and Fauvarque J F 2003 Electrochemical Characteristics and Impedance Spectroscopy Studies of Carbon-Carbon Supercapacitors *J. Electrochem. Soc.* **150** A292
- [30] Islam N, Hoque M N F, Li W, Wang S, Warzywoda J and Fan Z 2019 Vertically edge-oriented graphene on plasma pyrolyzed cellulose fibers and demonstration of kilohertz high-frequency filtering electrical double layer capacitors *Carbon N. Y.* **141** 523–30
- [31] Nathan-Walleser T, Lazar I, Fabritius M, Tölle F J, Xia Q, Bruchmann B, Venkataraman S S, Schwab M G and Mülhaupt R 2014 3D Micro-Extrusion of Graphene-based Active Electrodes: Towards High-Rate AC Line Filtering Performance Electrochemical Capacitors *Adv. Funct. Mater.* **24** 4706–16
- [32] Xue J, Gao Z, Xiao L, Zuo T, Gao J, Li D and Qu L 2020 An Ultrafast Supercapacitor Based on 3D Ordered Porous Graphene Film with AC Line Filtering Performance *ACS Appl. Energy Mater.* **3** 5182–9

- [33] Tang H, Xia K, Lu J, Fu J, Zhu Z, Tian Y, Wang Y, Liu M, Chen J, Xu Z, Guo Y, Khatoon R, Chen H and Ye Z 2021 NiTe₂-based electrochemical capacitors with high-capacitance AC line filtering for regulating TENGs to steadily drive LEDs *Nano Energy* **84** 105931
- [34] Claramunt S, Varea A, López-Díaz D, Velázquez M M, Cornet A and Cirera A 2015 The Importance of Interbands on the Interpretation of the Raman Spectrum of Graphene Oxide *J. Phys. Chem. C* **119** 10123–9
- [35] Kaniyoor A and Ramaprabhu S 2012 A Raman spectroscopic investigation of graphite oxide derived graphene *AIP Adv.* **2** 32183
- [36] Choi D, Blomgren G E and Kumta P N 2006 Fast and Reversible Surface Redox Reaction in Nanocrystalline Vanadium Nitride Supercapacitors *Adv. Mater.* **18** 1178–82
- [37] Kafizas A, Hyett G and Parkin I P 2009 Combinatorial atmospheric pressure chemical vapour deposition (cAPCVD) of a mixed vanadium oxide and vanadium oxynitride thin film *J. Mater. Chem.* **19** 1399

SUPLLEMENTARY FILE

One-step Pulsed Laser Deposition of Metal oxynitride/Carbon Composites for Supercapacitor Application

Subrata Ghosh*, Massimiliano Righi, Giacomo Pagani, Chengxi Hou, Valeria Russo, Carlo S. Casari*

Micro and Nanostructured Materials Laboratory - NanoLab, Department of Energy, Politecnico de Milano, via Ponzio 34/3, Italy

Keywords: Pulsed Laser Deposition; Metal oxynitride; Carbon; Nanocomposite; Supercapacitor

Corresponding authors Email: subrata.ghosh@polimi.it or subrata.ghoshk@rediffmail.com (Subrata Ghosh) and carlo.casari@polimi.it (Carlo S. Casari)

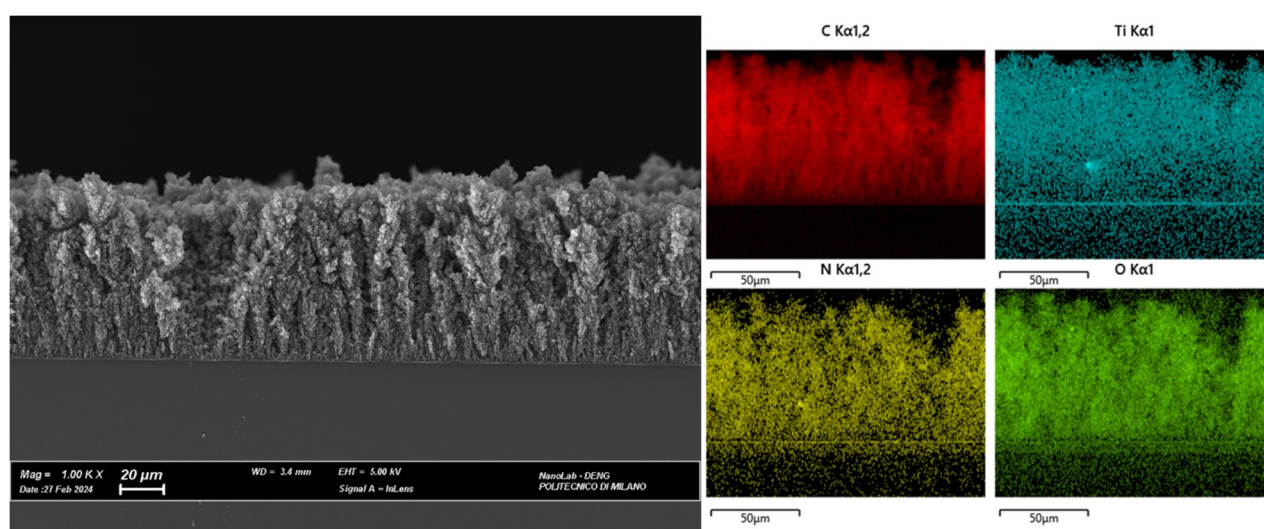


Figure S1: Cross-sectional scanning electron micrograph and elemental mapping of C-TiO_xN_y-1

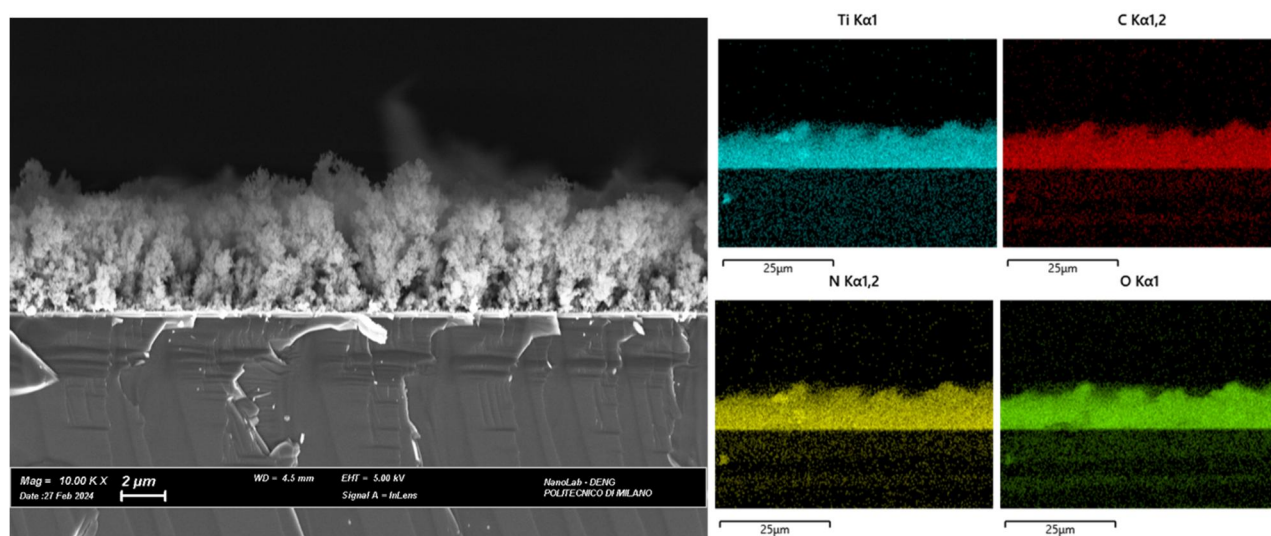


Figure S2: Cross-sectional scanning electron micrograph and elemental mapping of C-TiO_xN_y-2

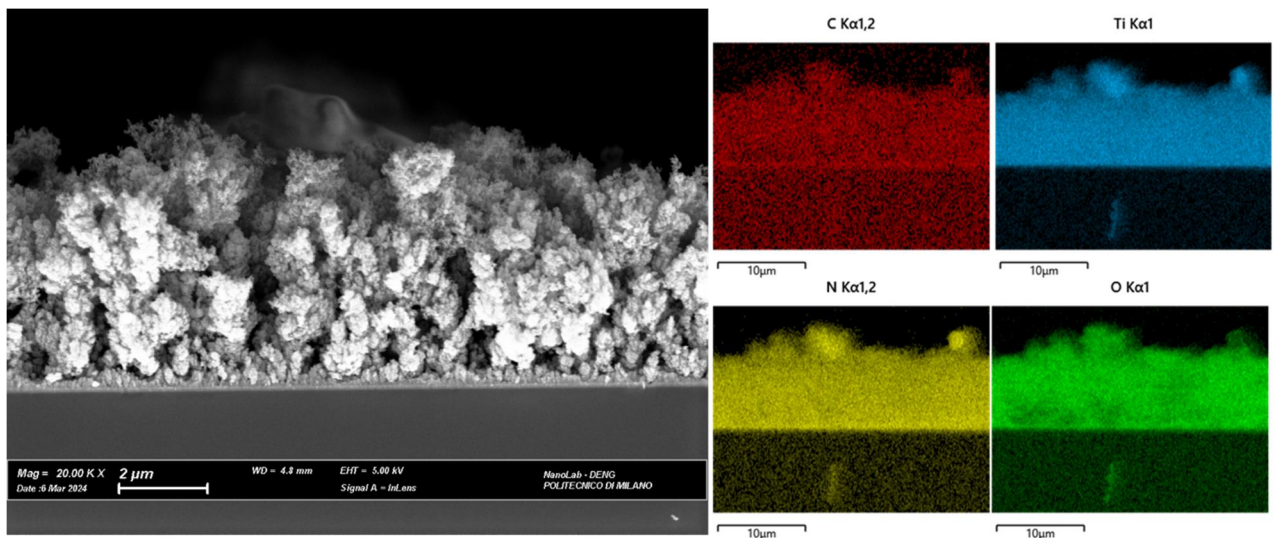


Figure S3: Cross-sectional scanning electron micrograph and elemental mapping of $C-TiO_xN_y-3$

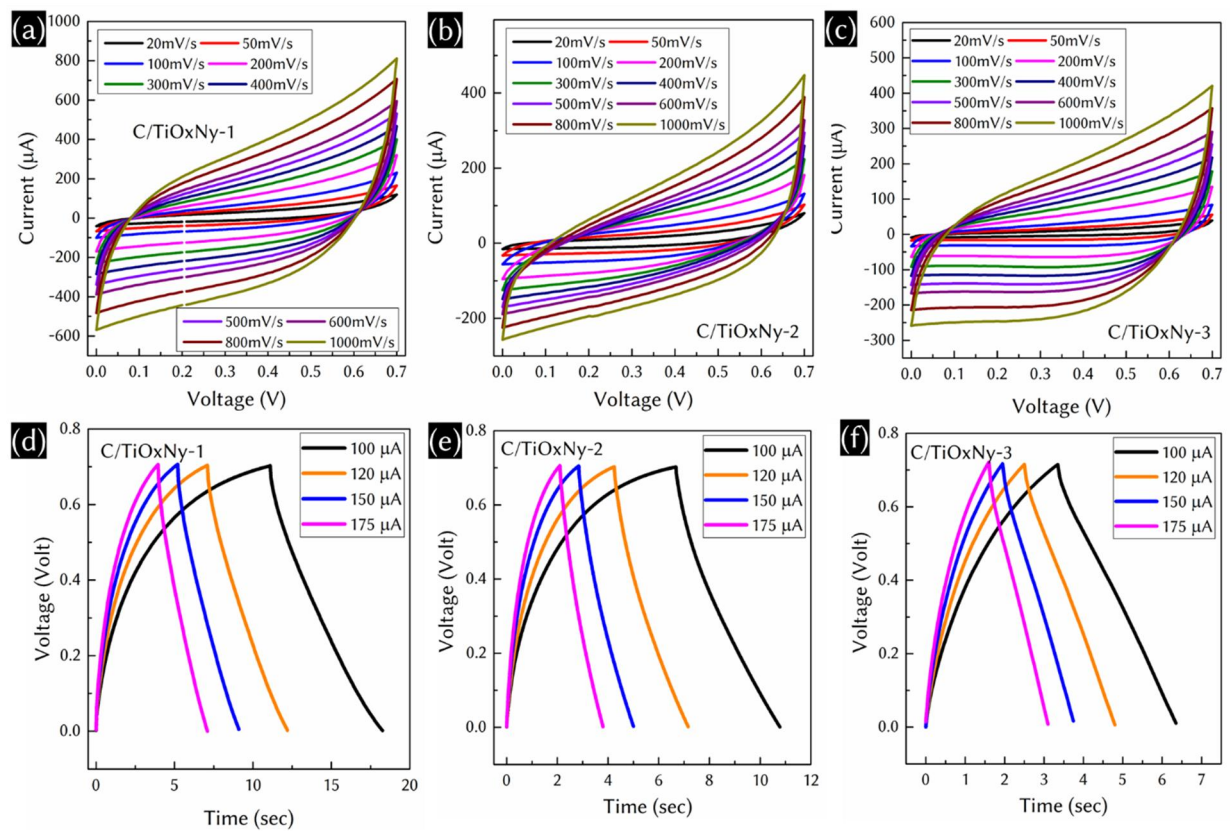


Figure S4: Cyclic voltammogram of (a) C/TiO_xN_y-1 , (b) C/TiO_xN_y-2 , and (c) C/TiO_xN_y-3 supercapacitor device at different scan rates. Charge-discharge profile of (a) C/TiO_xN_y-1 , (b) C/TiO_xN_y-2 , and (c) C/TiO_xN_y-3 supercapacitor device at different current densities.